coatings

MDPI

Article

Formation and Electrochemical Properties of Heterostructured Electrodes Based on Cu_2O and $CuCo_2O_4$

Anna A. Murashkina [1], Aida V. Rudakova [1,2], Tair V. Bakiev [1], Alexei V. Emeline [1,2,*] and Detlef W. Bahnemann [1]

[1] Laboratory of Photoactive Nanocomposite Materials, Saint Petersburg State University, 199034 Saint-Petersburg, Russia; murashkinaaa@mail.ru (A.A.M.); aida.rudakova@spbu.ru (A.V.R.); tairbakiev@gmail.com (T.V.B.); detlef.bahnemann@spbu.ru (D.W.B.)
[2] Department of Photonics, Saint Petersburg State University, 199034 Saint-Petersburg, Russia
* Correspondence: alexei.emeline@spbu.ru

Abstract: Individual (FTO/Cu_2O and FTO/$CuCo_2O_4$) and heterostructured (FTO/$BiVO_4$/Cu_2O, FTO/$BiVO_4$/$CuCo_2O_4$, and FTO/$CuCo_2O_4$/Cu_2O) electrodes were successfully formed using the electrodeposition method on copper-containing compounds. The morphology of the synthesized electrode systems, which affect the electrochemical properties, was determined. A comparative study of the electrochemical and photoelectrochemical properties of the individual and heterostructured electrodes showed that the modification of the $BiVO_4$ electrode surface with Cu_2O and $CuCo_2O_4$ oxides led to a significant increase in its efficiency as a photoanode. The deposition of Cu_2O nanoclusters onto $CuCo_2O_4$ nanoflakes increased the electrochemical stability of the electrode while maintaining its high capacitance.

Keywords: electrodeposition; nanostructures; surface modification; electrochemistry; $BiVO_4$; Cu_2O; $CuCo_2O_4$

Citation: Murashkina, A.A.; Rudakova, A.V.; Bakiev, T.V.; Emeline, A.V.; Bahnemann, D.W. Formation and Electrochemical Properties of Heterostructured Electrodes Based on Cu_2O and $CuCo_2O_4$. *Coatings* **2024**, *14*, 141. https://doi.org/10.3390/coatings14010141

Academic Editors: Emerson Coy and Rosalba Passalacqua

Received: 29 November 2023
Revised: 17 January 2024
Accepted: 18 January 2024
Published: 20 January 2024

1. Introduction

Heterostructured electrode materials are becoming an increasingly promising perspective in the development of technologies for energy production and storage [1–6]. The combination of individual semiconductor materials leads not only to the improvement of their functional properties but also to the creation of completely new active materials with unique properties due to the effective charge carrier separation at the heterojunction interface. As a result, it is possible to increase the efficiency and selectivity of the heterostructured materials in various electrochemical, catalytic, and photocatalytic processes, improve their chemical stability, and change their optical properties. It is wise to mention that an important criterion in the development of such materials is their low cost, simplicity, and the high reproducibility of the preparation method.

The formation of heterostructured materials results in the formation of the interfaces [7], where contact resistance arises, depending on the nature of the interaction between the component compounds, and is determined by the synthesis route of the layer formation. There are many different methods of synthesis and formation of heterostructured electrode systems possessing their advantages and disadvantages [8,9]. In the case of a component layer deposition from a suspension, the contact area of the two phases is limited by the particle size, while the coating formation via sol-gel technology promotes the formation of a uniform coating. Electrodeposition produces a dense micro-architectured film [7,10]. Changes in electrolyte composition (pH, concentration, and precursor) and/or electrodeposition parameters (temperature, potential, etc.) allow varying the surface morphology, film density, and thickness, influencing the size and crystallographic orientation of crystallites, as well as the composition of the film [11–13].

In the present studies, bismuth vanadate ($BiVO_4$), copper (I) oxide (Cu_2O), and copper (II) cobaltate ($CuCo_2O_4$) were selected as components of heterostructured electrode

systems. Due to the value of the band gap, E_g (2.4–2.5 eV), and the position of the valence band and the conduction band, which provides a high oxidative potential at excitation by visible light, bismuth vanadate is well established as an *n*-type semiconductor in various heterostructured systems [14,15]. The copper-containing compounds are often used as a heterostructure component providing a sufficient reduction potential for target reactions such as (photo) electrochemical reduction of CO_2 or production of H_2. For example, copper (I) oxide possesses a band gap E_g of ~2.0 eV and a reduction potential position higher than that of $BiVO_4$ [16]. Copper (II) cobaltate (E_g 1.4–1.8 eV) has also recently been actively studied for various applications, for example, as an electrocatalytic material or anode material of lithium-ion batteries [17–19]. As previously reported [20], the copper cobaltate synthesis method affects its physicochemical characteristics. Powdered copper cobaltate obtained from the hydrothermal synthesis method has a relatively low conductivity, specific capacitance, and electrochemical stability, while the formation of heterostructured $CuCo_2O_4$/CuO by sonochemistry using cetyltrimethylammonium bromide (CTAB) leads to an improvement in these properties compared to pure copper cobaltate [21].

The purpose of this study was to form and characterize single- and two-component electrode systems based on $BiVO_4$, Cu_2O, and $CuCo_2O_4$ by electrochemical deposition of copper-containing compounds, as well as a comparative study of their electrochemical and photoelectrochemical behavior.

2. Materials and Methods

Electrodes based on $BiVO_4$ material were formed by drop-casting a solution of bismuth vanadate precursors onto fluorine-doped tin oxide substrates (FTO glass, 25 mm × 25 mm and a surface resistance of < 100 Ohm/cm) [22,23]. For preparation, the solution was taken in a stoichiometric ratio of bismuth (III) nitrate pentahydrate $Bi(NO)_3 \cdot 5H_2O$ and vanadyl acetylacetonate $VO(C_5H_7O_2)_2$, which was dissolved in a mixture of glacial acetic acid and acetylacetone (20/1) with stirring for 1 h. Films were obtained by uniformly distributing the solution (70–80 μL) onto the surface of pre-cleaned FTO conductive substrates (2.5 × 2.5 cm^2) at room temperature, followed by the solvent removal at 100 °C within 30 min in the vacuum desiccator, and then further annealing at 450 °C for 3 h (the heating/cooling rate was 60°/h).

The preparation of Cu_2O layers was carried out by electrodeposition on conductive FTO substrates from an aqueous solution (pH 6.5), containing 0.1 M of sodium acetate CH_3COONa and 0.01 M of copper (II) acetate $Cu(CH_3COO)_2$ using a three-electrode electrochemical cell with the potentiostatic mode (Elins-Pro potentiostat) at −0.245 V relative to the potential of the Ag/AgCl reference electrode; a platinum plate was used as a counter electrode [24–26]. After deposition, the prepared sample was washed with distilled water, dried in air, and annealed in an oven at 300 °C for 20 min followed by rapid cooling to room temperature.

$CuCo_2O_4$ films were prepared by electrodeposition onto FTO substrates from an aqueous solution containing 10 mM of cobalt nitrate $Co(NO_3)_2$ and 2.5 mM of copper (II) nitrate $Cu(NO_3)_2$ in a three-electrode cell with a platinum plate as a counter electrode and the Ag/AgCl reference electrode [27]. Electrodeposition was carried out in a potentiostatic mode (Elins-Pro potentiostat) at −1.0 V relative to the potential of the Ag/AgCl electrode at room temperature for various times (not longer than 8 min). After electrochemical deposition, the $CuCo_2O_4$ layer was washed with distilled water, dried at room temperature, and then annealed in the oven at 400 °C in an air atmosphere for 2 h (the heating/cooling rate was 100°/h).

The Cu_2O and $CuCo_2O_4$ layers, as components of heterostructured electrodes FTO/$CuCo_2O_4$/Cu_2O, FTO/$BiVO_4$/Cu_2O, and FTO/$BiVO_4$/$CuCo_2O_4$, were electrodeposited onto the layers of the semiconductor materials (FTO/$BiVO_4$ and FTO/$CoCu_2O_4$), formed as described above.

The phase composition of coatings was determined by X-ray diffraction on a Bruker "D8 DISCOVER" high-resolution diffractometer (Germany) with CuKa radiation in the angle range of $20^\circ \leq 2\theta \leq 80^\circ$ and with a scanning speed of 5.0°/min. The phase reference data was taken from the ICDD database.

The surface morphology of the samples was studied using scanning electron microscopy (SEM) with a Zeiss Crossbeam 1540XB and Zeiss Merlin microscope with the Oxford Instruments INCAx-act (Carl Zeiss, Oberkochen, Germany) setup for elemental analysis by energy dispersion X-ray spectroscopy (EDX).

Electrochemical measurements were performed in a three-electrode electrochemical cell using an Elins-50 Pro potentiostat. The platinum plate and Ag/AgCl electrode were used as counter and reference electrodes, respectively, and a 0.2 M aqueous solution of potassium sulfate K_2SO_4 (pH 6.98) was used as the electrolyte. During cyclic voltammetry (CV) measurements, the scan rate was 15 mV/s. The scan rate-dependent voltammetric currents for $CuCo_2O_4$-containing electrodes were recorded at potential scan rates ranging from 5 to 110 mV/s. The galvanostatic charge-discharge measurements (GCD) were tested within the potential window of −0.4 to 0.4 V at the current densities ranging from 1 to 9 A/g. The long-term stability of the $CuCo_2O_4$-containing electrodes was carried out by GCD measurements for 500 cycles at the current density, matched with the highest value of the specific capacitance of electrodes. The Mott-Schottky dependencies were registered at 10 and 100 Hz (amplitude was 10 mV).

In photoelectrochemical studies, the irradiation of the electrodes was carried out using a 300-W Xenon Lamp (Oriel Instruments), the light irradiance was 100 mW/cm^2.

3. Results and Discussion

3.1. Characterization

The formation of copper-containing layers was monitored by the time evolution of the current density (*j*) in the cathodic deposition process. The kinetic dependences of the current density during the deposition of Cu_2O and $CuCo_2O_4$, both on pure conductive substrates and substrates with deposited electrode layers of $BiVO_4$ and $CuCo_2O_4$, are presented in Figure 1. As evident from the presented data, the current density values at the initial and stationary stages were different for different samples.

The morphology of the electrodepositing layers was studied using scanning electron microscopy (SEM). The surface images of the electrodes were taken after 50, 100, and 400 s of the electrodeposition process (Figure 2).

It is known [24,28,29] that the process of the electrochemical formation of copper (I) oxide can be presented as a two-step process, including the stages of the reduction of Cu^{2+} ions to Cu^+ ions and the deposition of Cu^+ from an aqueous solution in the form of Cu_2O:

$$Cu^{2+} + e \rightarrow Cu^+$$

$$2Cu^+ + H_2O \rightarrow Cu_2O + 2H^+$$

or as a one-step process directly reducing Cu^{2+} ions to Cu_2O involving two electrons:

$$2Cu^{2+} + H_2O + 2e \rightarrow Cu_2O + 2H^+.$$

A certain electrochemical reaction pathway depends on factors such as the applied potential, the source of the copper (II) ion, the pH and temperature of the solution, and the type of substrate [24,30–32]. The stabilization of the copper ions in the oxidation state (I) at the potentiostatic deposition mode (the applied potential was −0.245 V, relative to the reference electrode) was carried out by maintaining the acidity of the solution at a pH of 6.5 and a temperature of 65 °C [25,26]. During the electrocrystallization of Cu_2O, the dependence of current density on time had similar characteristics for the processes of deposition of the material onto both the FTO substrate and substrates with $BiVO_4$ and $CuCo_2O_4$ coatings. Namely, a slight increase in the current density at the initial moment

and a gradual decay of the current density by approximately 0.4 mA/cm^2 (indicating the increase in resistance) with an increased time of deposition was observed (Figure 1).

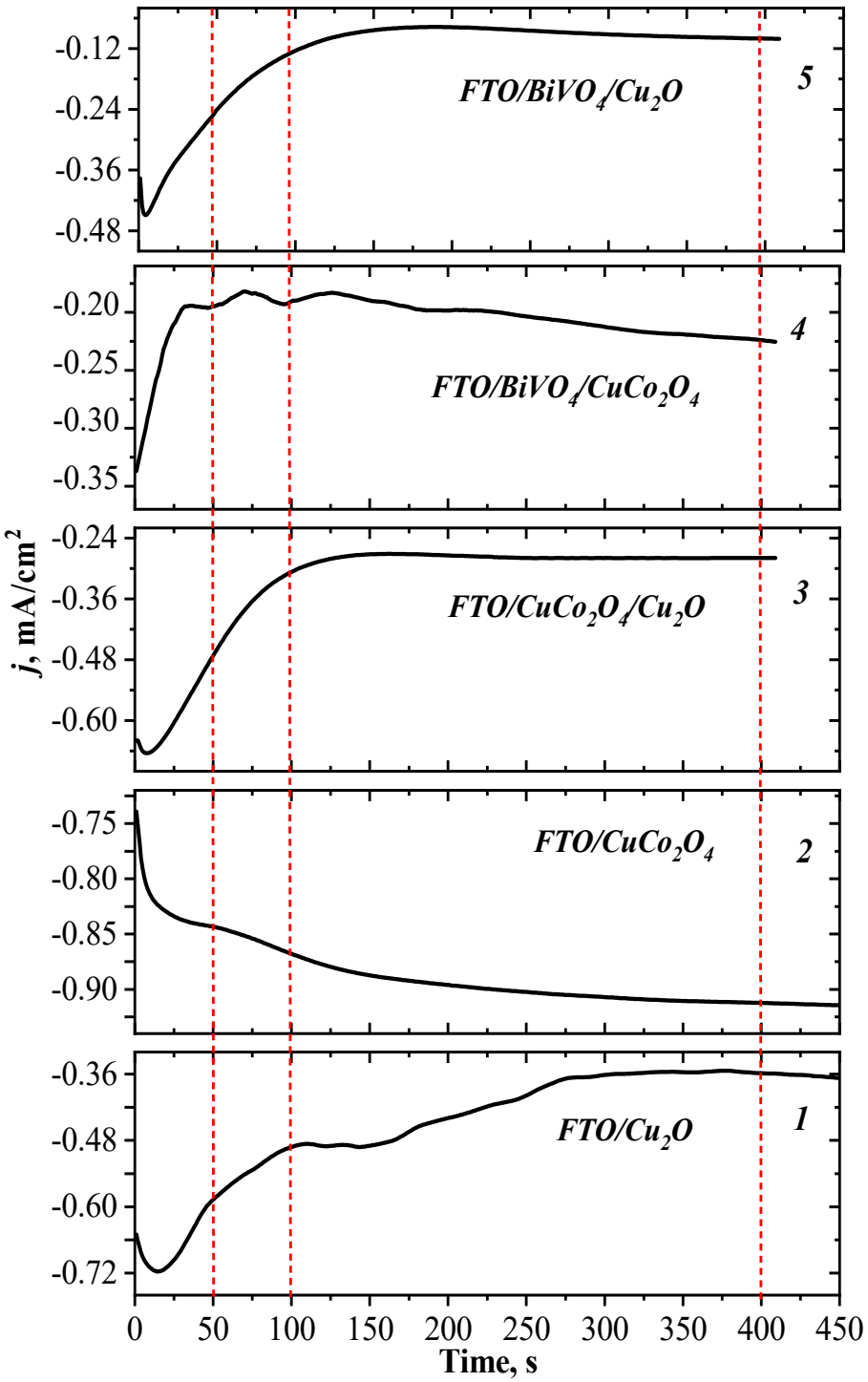

Figure 1. Dependences of current density on electrodeposition time for individual electrodes FTO/Cu_2O (1) and FTO/$CuCo_2O_4$ (2), and heterostructured materials, FTO/$CuCo_2O_4$/Cu_2O (3), FTO/$BiVO_4$/$CuCo_2O_4$ (4), and FTO/$BiVO_4$/Cu_2O (5). Red dotted lines indicate process times for monitoring electrode layer formation by SEM (see Figure 2).

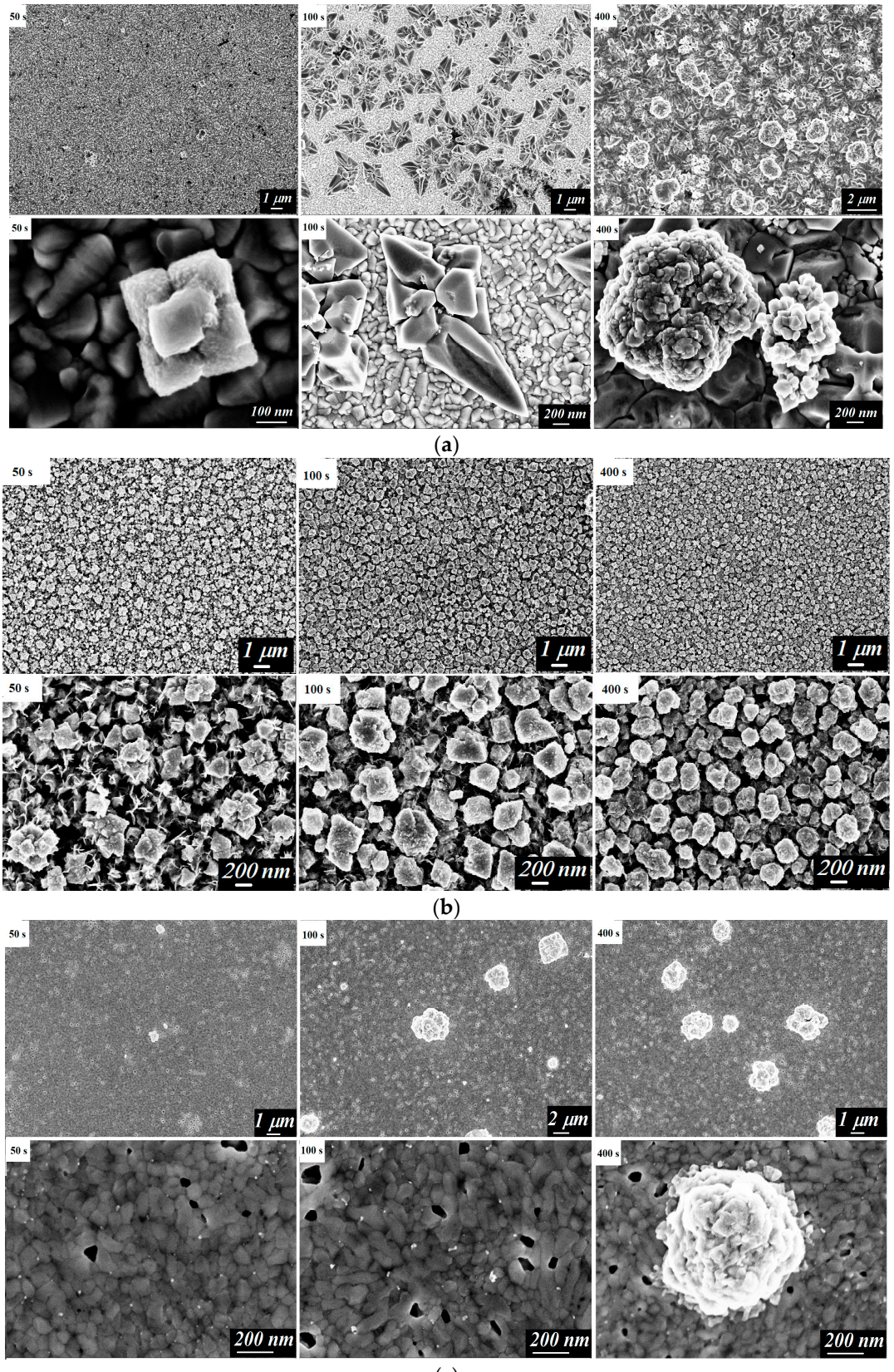

Figure 2. *Cont.*

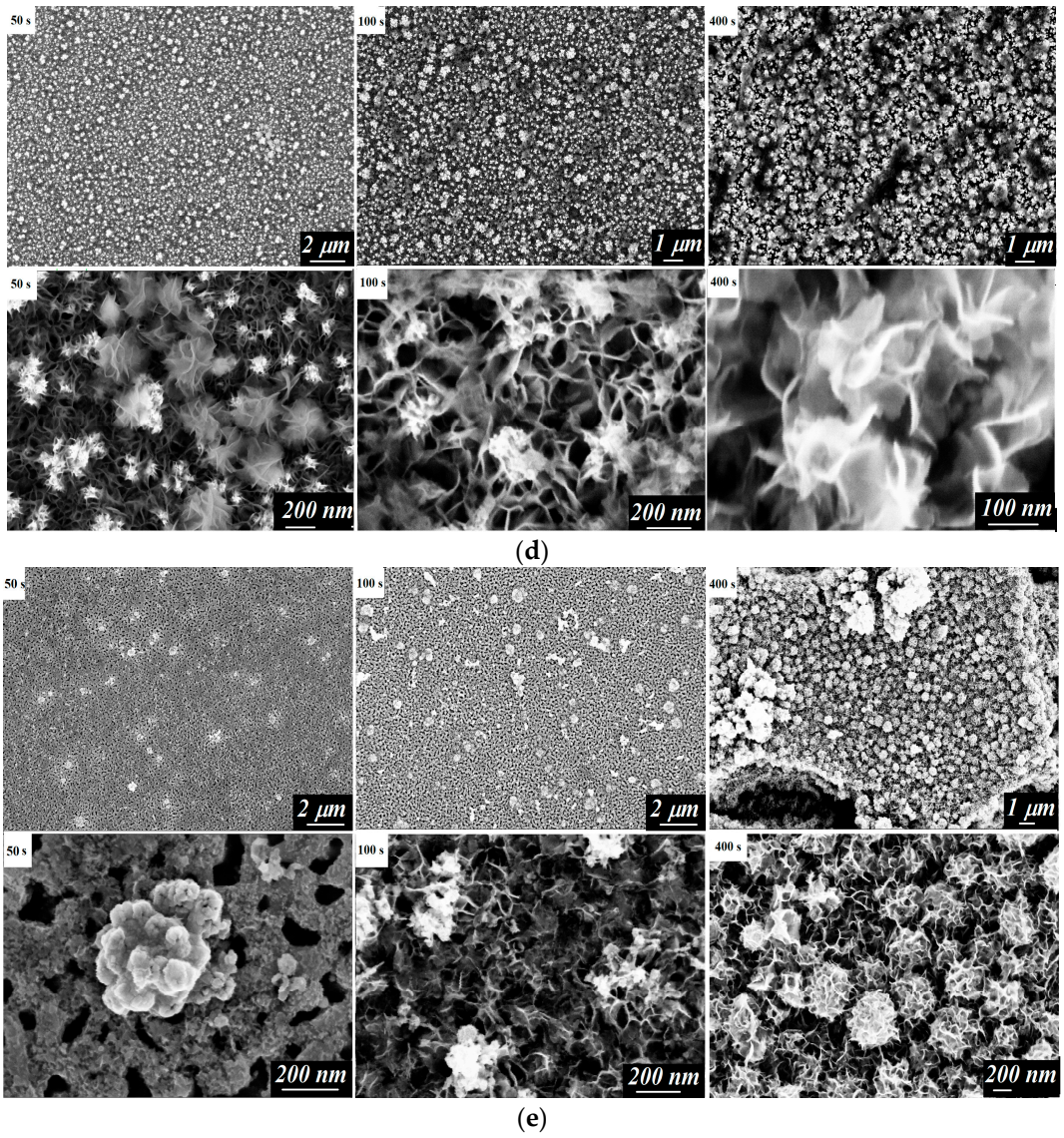

Figure 2. SEM images of the surface of the studied electrodes: FTO/Cu_2O (**a**), FTO/$CuCo_2O_4$/Cu_2O (**b**), FTO/$BiVO_4$/Cu_2O (**c**), FTO/$CuCo_2O_4$ (**d**), and FTO/$BiVO_4$/$CuCo_2O_4$ (**e**) after electrodeposition for 50 s, 100 s, and 400 s.

The Cu_2O formation process depended on the type of substrate, as demonstrated by microscopic images of the surface of the FTO/Cu_2O, FTO/$CuCo_2O_4$/Cu_2O, and FTO/$BiVO_4$/Cu_2O samples during deposition (Figure 2a–c). On the smooth surface of FTO glasses, at the initial step of the deposition, individual nuclei appeared that were 200–300 nm in size. In further time evolution, these nuclei appeared on the entire surface, and, after that, the agglomerates of particles with a size larger than 1 μm were formed.

A similar scenario was observed during the formation of the Cu_2O phase on the $BiVO_4$ dense layer with a thickness of about 400–450 nm (Figure 2c). However, in this case, the copper (I) oxide nuclei of noticeably smaller sizes (10–20 nm) grew into agglomerates of particles up to 1 μm, without forming a uniform layer of Cu_2O on the bismuth vanadate surface.

The synthesis of $CuCo_2O_4$ occurs through the formation of bimetallic (Cu, Co) hydroxide on the substrate surface due to the interaction of Cu^{2+} and Co^{2+} ions from a solution, with hydroxide ions formed during the reduction of NO_3^- ions on the cathode [27,33]:

$$NO_3^- + 7H_2O + 8e \rightarrow NH_4^+ + 10OH^-$$

$$xCu^{2+} + 2xCo^{2+} + 6xOH^{-} \rightarrow Cu_xCo_{2x}(OH)_{6x}.$$

The resulting hydroxide is converted to $CuCo_2O_4$ by annealing at 400°C in an air atmosphere:

$$Cu_xCo_{2x}(OH)_{6x} + 1/2xO_2 \rightarrow xCuCo_2O_4 + 3xH_2$$

The electrocrystallization process of the $CuCo_2O_4$ pre-phase was characterized by an increased current density within the first 50 s (Figure 1), corresponding to the formation of $Cu_xCo_{2x}(OH)_{6x}$. In the SEM images of the material surface, the formation of nanoflakes (Figure 2d) was observed. A similar characteristic form of the $CuCo_2O_4$ film has been demonstrated elsewhere [27]. With an increased deposition time of up to 100–200 s, the process was characterized by a small change in the current density. According to microphotographs, a uniform layer of the $CuCo_2O_4$ nanoflakes was formed.

The formation of a $Cu_xCo_{2x}(OH)_{6x}$ phase on the $BiVO_4$ layer was accompanied by the formation of electrodeposition centers that led to sharp decay of the current density for the first 10 s (Figure 2e). The further co-deposition of Cu^{2+} and Co^{2+} ions occurred at the stable stationary value of the current density and resulted in the formation of a uniform layer of material with a developed surface morphology in the form of nanoflakes (Figures 1 and 2e).

On the surface of the $CuCo_2O_4$, with the developed morphology represented by a network of nanoflakes (Figure 2d), copper (I) oxide already covered the substrate with a uniform layer at short electrodeposition times (Figure 2b). This corresponded to the plateau of the current density curve (Figure 1). Further electrodeposition of copper (I) oxide led to the formation of agglomerates. Under the selected electrodeposition and annealing conditions, a dense electrode layer of Cu_2O with a thickness of about 1 μm was formed.

Thus, the developed surfaces of $BiVO_4$ and $CuCo_2O_4$ layers had a larger number of crystallization centers compared to the smooth surface of the FTO substrate, which accelerated the process of the formation of the Cu_2O layer. The current stabilization time during the Cu_2O electrodeposition process was approximately two times shorter in the case of deposition on the sub-layers of $BiVO_4$ and $CuCo_2O_4$ than on the FTO substrate (Figure 1).

The phase composition of the formed electrodes was determined by XRD (Figure 3). The phase of the electrodes FTO/Cu_2O and FTO/$BiVO_4$/Cu_2O corresponded to the individual Cu_2O phase (card No. 01-071-3645, ICDD), and the monoclinic phase of $BiVO_4$ (clinobisvanite, card No. 01-072-1465, ICDD) (Figure 3a).

The phase analysis of $CuCo_2O_4$ was difficult since the relative intensities of mixed oxide diffraction lines with face-centered cubic structures matched well with the diffraction pattern for cobalt spinel Co_3O_4. For $CuCo_2O_4$, diffraction peaks were observed at 31.09°, 36.64°, 44.55°, 59.00° and 64.83° (Figure 3b), which agrees well with the 2θ values for the (220), (311), (400), (511) and (440) planes, respectively, for cobalt spinel Co_3O_4 [34]. However, the cell parameter, a = 8.1289 Å, obtained for our sample was in good agreement with the values 8.133 Å and 8.12 Å, defined for $Cu_{0.95}Co_{2.05}O_4$ [34] and $CuCo_2O_4$ [35], respectively, and sufficiently larger than the value of 8.09 Å, determined for Co_3O_4 [35]. At the same time, the analysis of the elemental composition by energy dispersion X-ray spectroscopy (EDX) showed the presence of copper and cobalt in the molar ratio of Cu:Co at ~1:2 (Figure S1, and Tables S1 and S2), which exactly corresponded to the composition of the copper cobaltate, $CuCo_2O_4$.

The presence of diffraction peaks belonging to the $CuCo_2O_4$ phase in the X-ray diffraction patterns of the FTO/$BiVO_4$/$CuCo_2O_4$ (Figure 3b) and FTO/$CuCo_2O_4$/Cu_2O (Figure 3c) electrodes confirmed the formation of this phase in heterostructured electrodes. The phase composition revealed small amounts of the secondary phases, $CuBi_2O_4$ and CuV_2O_5, observed for the FTO/$BiVO_4$/$CuCo_2O_4$ electrode after annealing, which was formed due to the interaction of bismuth vanadate and copper (II) ions at the interface.

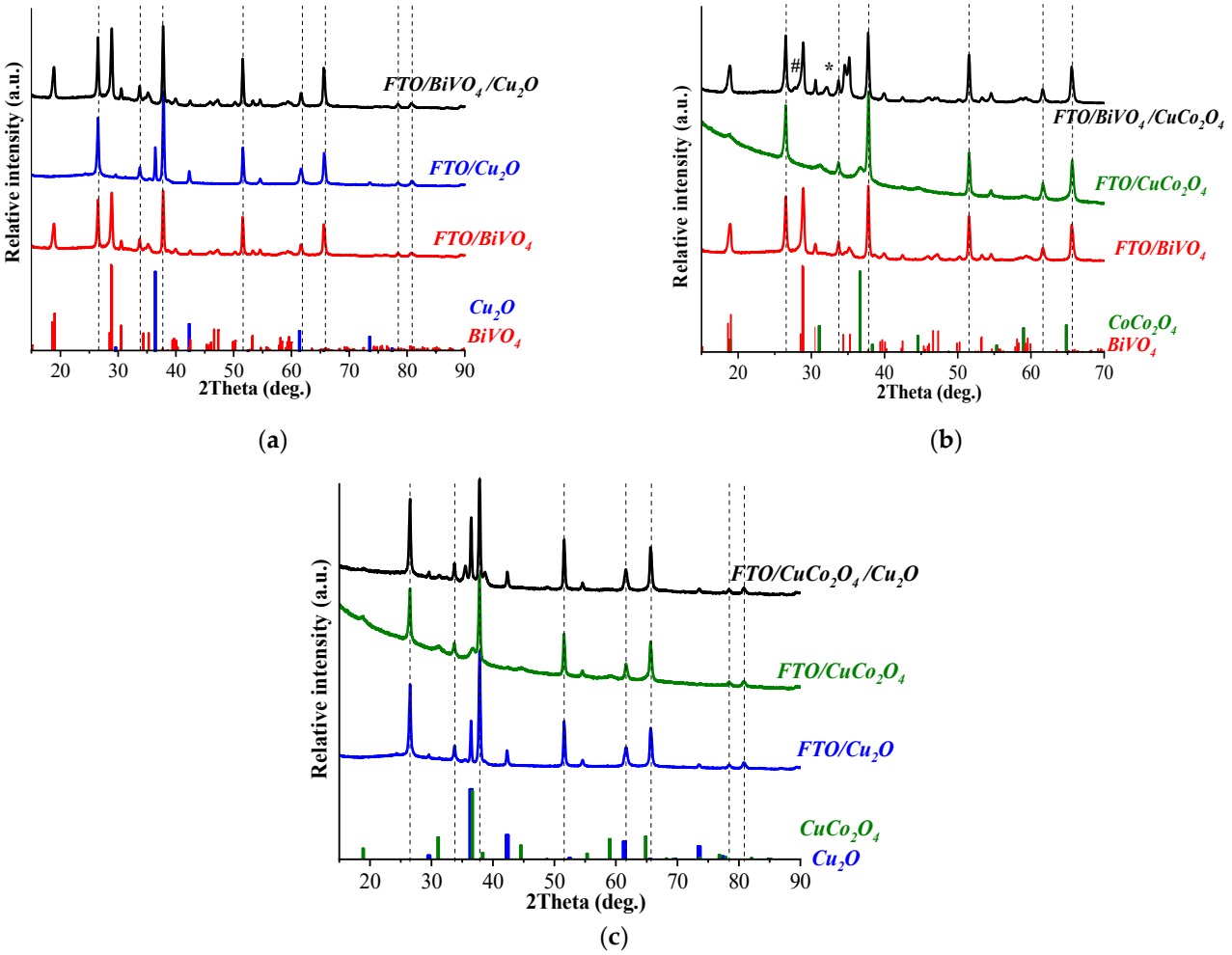

Figure 3. X-ray diffraction patterns of individual electrodes and heterostructured materials based on Cu_2O and $BiVO_4$ (**a**), $CuCo_2O_4$ and $BiVO_4$ (**b**), and Cu_2O and $CuCo_2O_4$ (**c**). Dashed lines indicate the reflection of the SnO_2 phase (Card No. 01-077-0452, ICDD). The colored lines mark the main reflections of the Cu_2O phases (in blue, card No. 01-071-3645), $BiVO_4$ phases (in red, card No. 01-072-1465), and $CoCo_2O_4$ phases (in green, card No. 00-080-1535), according to the ICDD database. Secondary phases $CuBi_2O_4$ and CuV_2O_5 are indicated by an asterisk (*) and a lattice (#), respectively.

3.2. Electrophysical and Electrochemical Properties

The type of conductivity in the synthesized samples was determined from Mott–Schottky plots (Figure 4). The dependencies for FTO/Cu_2O (a) and FTO/$CuCo_2O_4$ (b) electrodes showed negative slopes, demonstrating the *p*-type conductivity of semiconductors. The positive slope for the FTO/$BiVO_4$ (c) electrode corresponded to the *n*-type of conductivity of this semiconductor.

The Mott–Schottky plots of the heterostructured electrodes FTO/$BiVO_4$/Cu_2O (d) and FTO/$CuCo_2O_4$/Cu_2O (f) demonstrated both positive and negative slopes at different potential ranges, which suggested a switching between the *n*-type and *p*-type conductivity of materials.

The Mott–Schottky plot of FTO/$BiVO_4$/$CuCo_2O_4$ (Figure 4f) showed the presence of several positive and negative slopes which could be due to the presence of additional phases in the heterostructured system that matched well with the results of the XRD analysis, demonstrating the formation of the secondary phases $CuBi_2O_4$ and CuV_2O_5 (Figure 3a).

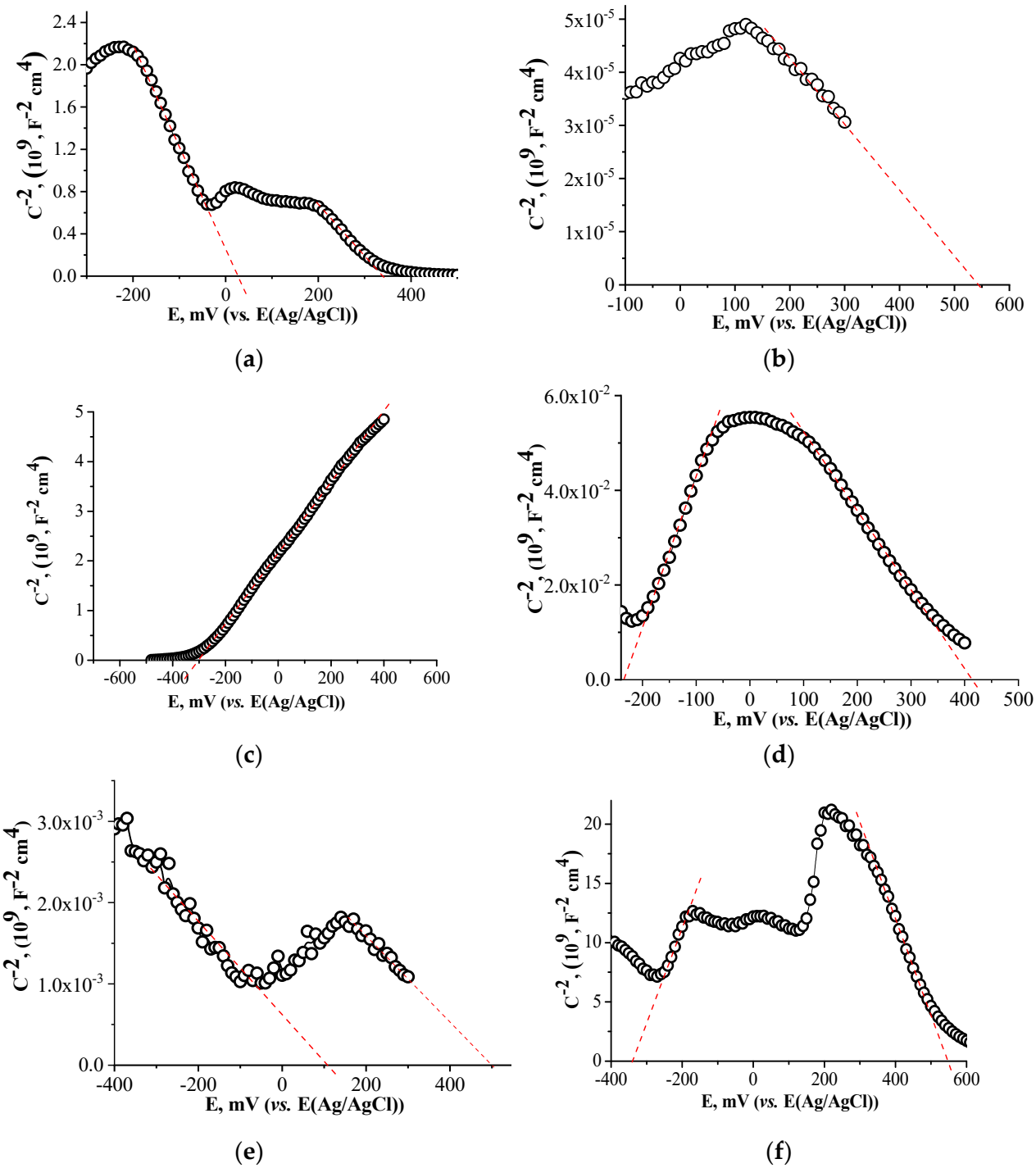

Figure 4. Mott–Schottky plots of electrodes: FTO/Cu_2O (**a**), FTO/$CuCo_2O_4$ (**b**), FTO/$BiVO_4$ (**c**), FTO/$BiVO_4$/Cu_2O (**d**), FTO/$CuCo_2O_4$/Cu_2O (**e**), FTO/$BiVO_4$/$CuCo_2O_4$ (**f**).

The Mott–Schottky plots also allow the determination of the flat band potentials, E_{fb}, by extrapolation of the slope to the x-axis. The corresponding E_{fb} values for the electrodes are presented in Table 1.

Figure 5 shows the cyclic current-voltage plots for all electrodes studied. The values of the onset potential on the anode branch of the plots are presented in Table 1.

Table 1. Values of flat band potential (E_{fb} vs. E(NHE)), the onset potential (E_{onset} vs. E(Ag/AgCl)), band gap (E_g), and maximum (j_{max}) and stationary-state (j_{st}) photocurrents for all studied materials.

Electrode	E_{fb}, V	E_{onset}, V	E_g, eV	j_{max}, μA/cm^2	j_{st}, μA/cm^2
FTO/$BiVO_4$	−0.08	0.19	2.6	1.83	0.34
FTO/Cu_2O	0.56	−0.08	2.4	−0.40	−0.04
FTO/$CuCo_2O_4$	0.76	−0.34	1.2	0.01	−0.03
FTO/$BiVO_4$/Cu_2O	0.63	−0.14		3.68	2.40
FTO/$BiVO_4$/$CuCo_2O_4$	0.77	−0.10		4.15	0.26
FTO/$CuCo_2O_4$/Cu_2O	0.72	−0.38		−0.09	−0.04

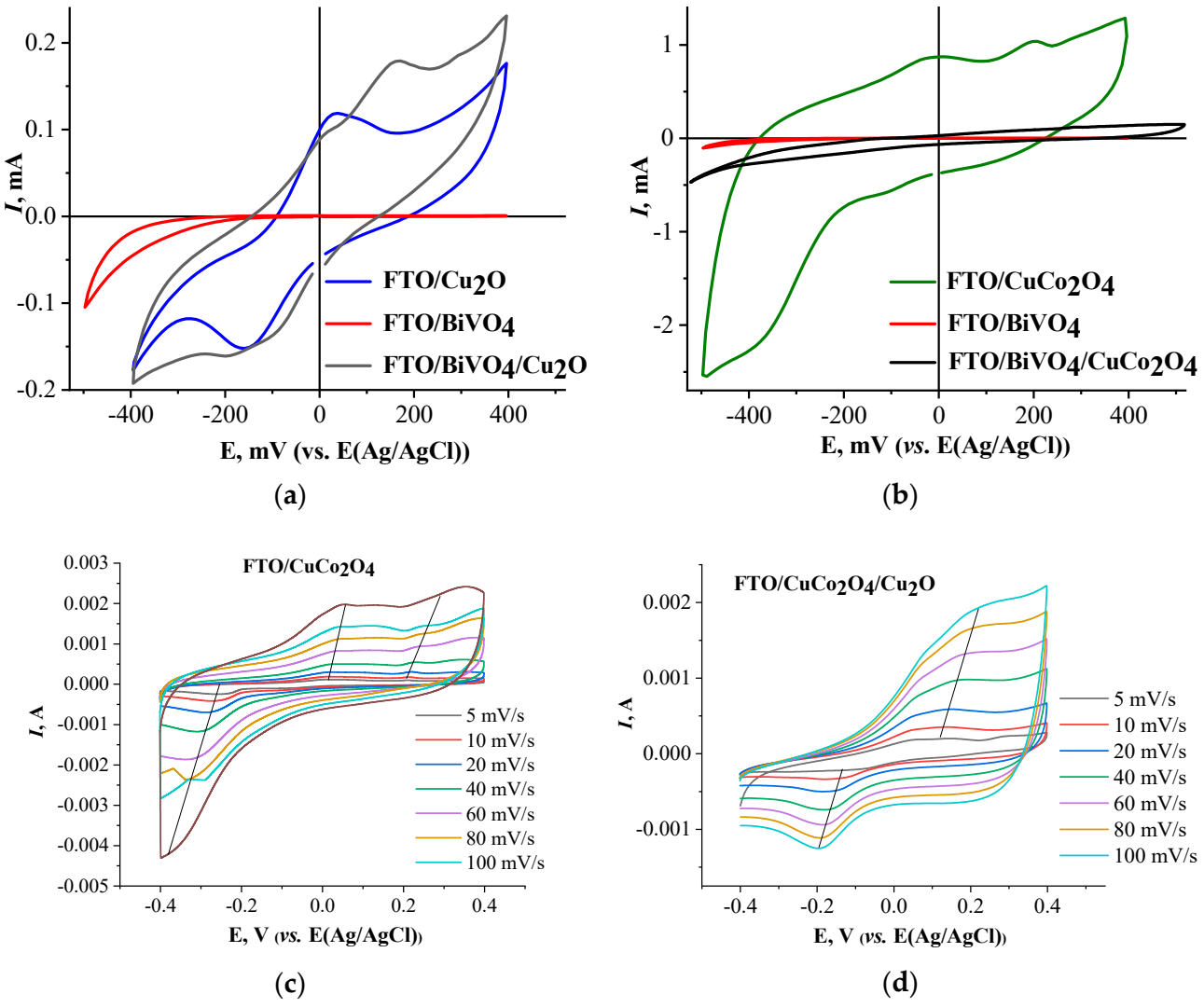

Figure 5. CV curves of individual and heterostructured electrodes: FTO/Cu_2O, FTO/$BiVO_4$, and FTO/$BiVO_4$/Cu_2O (**a**), FTO/$CuCo_2O_4$, FTO/$BiVO_4$, and FTO/$BiVO_4$/$CuCo_2O_4$ (**b**) at a scan rate of 15 mV/s; FTO/$CuCo_2O_4$ (**c**) and FTO/$CuCo_2O_4$/Cu_2O (**d**) at a scan rate ranging from 5 to 100 mV/s.

A characteristic hysteresis was observed on the forward and reverse branches of the current-voltage plot for all Cu_2O-containing electrodes, which was attributed to the occurrence of redox reactions involving Cu^+ and Cu^{2+}. In the potential range from −0.4 to 0.4 V for the Cu_2O electrode, one anodic peak was observed at 0.03 V and one cathodic peak at −0.15 V, vs. the Ag/AgCl electrode potential, which corresponded to the oxidation of Cu_2O and the reduction of CuO, respectively. Similar features were observed for the Cu_2O electrode elsewhere [30,36–38]. In the case of the deposition of Cu_2O on $BiVO_4$, in

the form of micro-clusters (Figure 2c), the CV-curve for the FTO/$BiVO_4$/Cu_2O electrode (Figure 5a) demonstrated an additional anodic peak at 0.16 V, which could be attributed to the dissolution process of Cu_2O according to the reaction:

$$Cu_2O + H_2O \rightarrow 2Cu^{2+} + 2e + 2OH^-.$$

Typically, this process occurs at potentials above 0.4 V for individual oxide electrodes [36].

As mentioned in the Introduction section, $CuCo_2O_4$-based electrodes can potentially be used in energy storage electrochemical systems. The FTO/$CuCo_2O_4$ and FTO/$CuCo_2O_4$/Cu_2O electrodes were characterized by CV measurements at a scan rate ranging from 5 to 100 mV/s to estimate the capacity of the electrodes. The CV plots (Figure 5c,d), in the range of −0.4 V to 0.4 V, demonstrated a significant hysteresis, which indicated a high capacity of the materials [39], with two insignificant peaks at −0.02 V and 0.20 V due to Red-Ox reactions involving copper ion pairs Cu^{2+}/Cu^+ and cobalt ion pairs Co^{4+}/Co^{3+} by the "charge-discharge" processes, which are typical for battery electrodes:

$$CuCo_2O_4 + H_2O + e \leftrightarrow 2CoOOH^- + Cu(OH)^+$$

$$2CoOOH^- + OH^- \leftrightarrow CoO_2 + H_2O + 2e$$

$$Cu(OH)^+ + e \leftrightarrow Cu(OH)$$

The observed linear shifts of the characteristic Red-Ox peaks with increasing scan rates indicated a diffusion-controlled behavior of the electrochemical processes [40]. In the field of high negative potentials, the reduction of Cu^+ or Cu^{2+} to Cu^0 is also possible. At a polarization up to −0.5 V, the spinel type (Co_3O_4) phase formation occurs on the surface of $CuCo_2O_4$ [41]. Thus, despite the high capacitance, the electrode material of $CuCo_2O_4$ is prone to degradation in accordance with previously published data [11,42,43].

The GCD dependencies obtained for the FTO/$CuCo_2O_4$ and FTO/$CuCo_2O_4$/Cu_2O electrodes (Figure S3) demonstrated a nonlinear character which is typical for battery-like behavior [44]. The maximal gravimetric capacities estimated from GCD dependencies were 540.0 F/g at 2 A/g for FTO/$CuCo_2O_4$ and 476.5 F/g at 1 A/g for FTO/$CuCo_2O_4$/Cu_2O electrodes. These data are in good agreement with results reported elsewhere [33,39]. Thus, Cu_2O deposition on the surface of the FTO/$CuCo_2O_4$ electrode insignificantly decreased its specific capacity. At the same time, the period of the charge-discharge process was shorter for the FTO/$CuCo_2O_4$/Cu_2O electrode.

The long-term stability of the $CuCo_2O_4$-based electrodes was verified by running 500 GCD cycles (Figure S4). The test results indicated that the specific capacity decayed to 40% in the first 100 cycles and then remained almost stable. It should be noted, that despite the lower initial specific capacity value detected for the FTO/$CuCo_2O_4$/Cu_2O electrode as compared to that for the FTO/$CuCo_2O_4$ electrode, at the end time of the test, the values for both electrodes were practically the same. This observation indicated a positive effect of Cu_2O deposition on the long-term stability of $CuCo_2O_4$-based electrodes.

The combination of copper cobaltate with bismuth vanadate (FTO/$BiVO_4$/$CuCo_2O_4$) significantly reduced the capacitive characteristics of the material and improved its electrochemical performance compared to FTO/$BiVO_4$ (Figure 5b).

In addition, the photoelectrochemical properties of the obtained electrode systems were tested. The chronoamperometric measurements were carried out in the electrochemical cell, without external bias, upon irradiation with the light of a xenon lamp ($\lambda > 300$ nm, $E < 4$ eV), which corresponds to the photoexcitation of all components in the heterostructured systems in their intrinsic absorption spectral regions (see Figure S2). Figure 6 shows the photocurrent evolution curves under irradiation. The peak and stationary-state photocurrent characteristics for all electrodes are shown in Table 1.

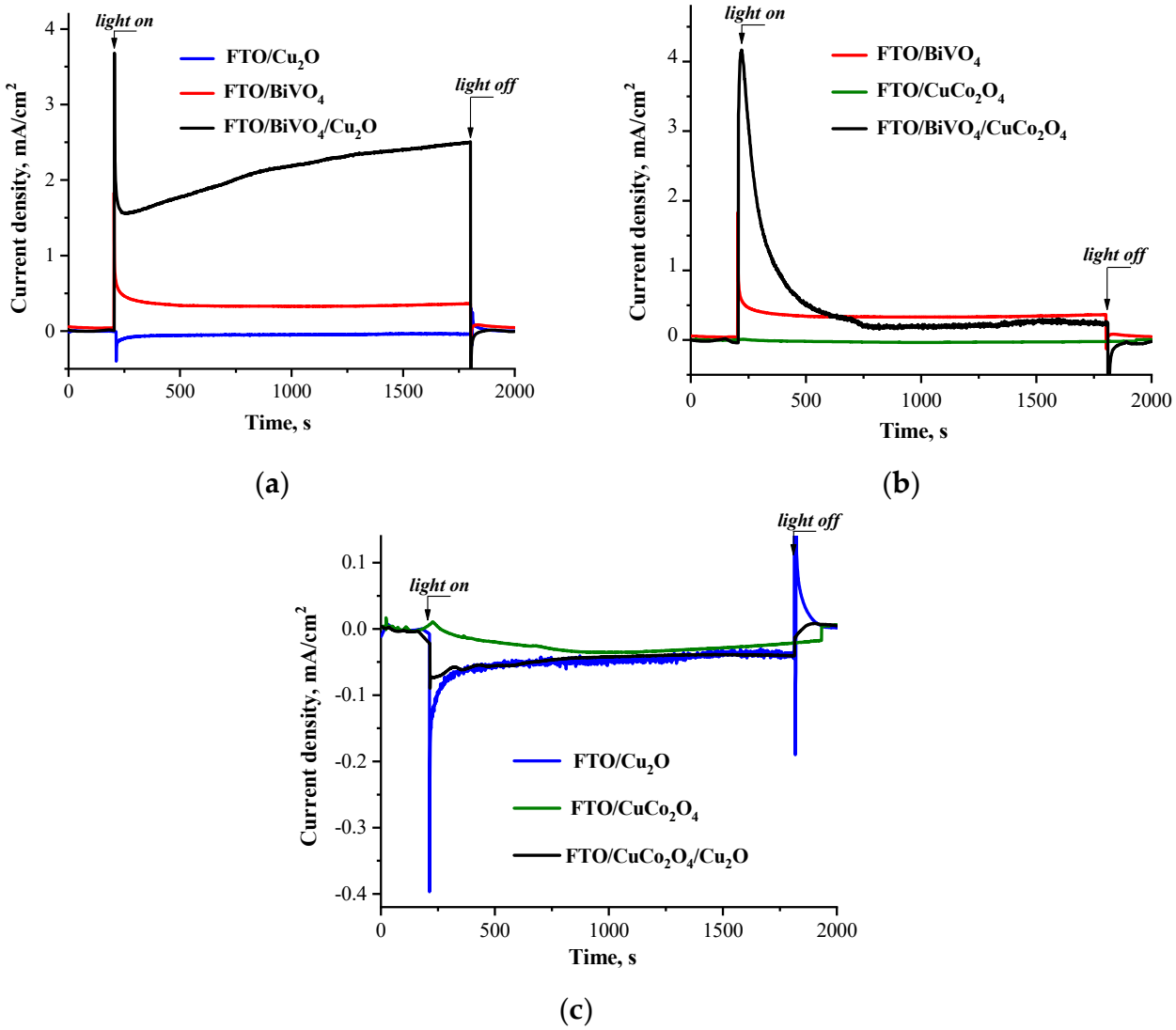

Figure 6. The kinetic dependencies of photocurrent for electrodes upon irradiation: FTO/Cu_2O, FTO/$BiVO_4$, and FTO/$BiVO_4$/Cu_2O (**a**); FTO/$CuCo_2O_4$, FTO/$BiVO_4$, and FTO/$BiVO_4$/$CuCo_2O_4$ (**b**); FTO/Cu_2O, FTO/$CuCo_2O_4$, and FTO/$CuCo_2O_4$/Cu_2O (**c**).

An anodic photocurrent was observed for the FTO/$BiVO_4$ electrode (Figure 6a,b), which corresponded to the electronic nature of bismuth vanadate as an *n*-type semiconductor according to the Mott–Schottky plot (Figure 4c). The Cu_2O electrode demonstrated a cathodic direction of photocurrent, but its photoresponse under the stationary-state condition reached only a few nA (Figure 6a,c). The same scenario was observed for the $CuCo_2O_4$ electrode, which was practically inactive under irradiation (Figure 6c). As noted above, the $CuCo_2O_4$ electrode material possessed a high capacity and conductivity, which did not result in a good photoresponse. The presence of Cu_2O on the surface of $CuCo_2O_4$ did not improve the photoactivity of the composite electrode.

The direction of the photocurrent for copper-containing electrodes demonstrated their photocathodic properties under irradiation. However, it changed to an anodic regime when copper-containing compounds were deposited on the surface of the bismuth vanadate substrate. The magnitude of the photocurrent for such a modified electrode was significantly higher than that for the individual $BiVO_4$ electrode.

4. Conclusions

It was demonstrated that individual and heterostructured electrodes based on Cu_2O and $CuCo_2O_4$ could be successfully formed by the electrodeposition method. The optimal time of the electrodeposition process was found to be 5 min. The Cu_2O phase was deposed on the bismuth vanadate layer in the form of separate nanoclusters. At the same time, $CuCo_2O_4$ particles were spread evenly over the surface as nanoflakes. The $CuCo_2O_4$ electrode demonstrated a high specific capacity with 53% of the initial value retained after 500 cycles. The electrochemical deposition of Cu_2O on its surface could potentially improve the charge-discharge cycle time and long-term stability. It was also demonstrated that the surface modification of the $BiVO_4$ electrode by either Cu_2O or $CuCo_2O_4$ resulted in a significant increase in its efficiency as a photoanode.

Supplementary Materials: The following supporting information can be downloaded at https://www.mdpi.com/article/10.3390/coatings14010141/s1: Figure S1: SEM images of FTO/$CuCo_2O_4$ surface; Figure S2: Tauc plots for Cu_2O, $CuCo_2O_4$ и $BiVO_4$; Figure S3: GCD curves of FTO/$CuCo_2O_4$ electrode and FTO/$CuCo_2O_4$/Cu_2O, specific capacitance *vs* current density for FTO/$CuCo_2O_4$ and FTO/$CuCo_2O_4$/Cu_2O; Figure S4: The cyclic performance of electrodes at the current density corresponding to maximum specific capacitance; Table S1: The EDX analysis data of the FTO/$CuCo_2O_4$ surface in Figure S1(a); Table S2: The EDX analysis data of the FTO/$CuCo_2O_4$ surface in Figure S1(b).

Author Contributions: Conceptualization, A.V.E. and A.V.R.; methodology, A.V.E. and A.V.R.; software, A.A.M. and A.V.R.; validation, A.A.M. and T.V.B.; formal analysis, A.A.M. and A.V.R.; investigation, A.A.M. and T.V.B.; resources, A.V.E. and D.W.B.; data curation, A.A.M., A.V.R. and A.V.E.; writing—original draft preparation, A.A.M.; writing—review and editing, A.V.R. and A.V.E.; visualization, A.A.M. and A.V.R.; supervision, A.V.E.; project administration, A.A.M.; funding acquisition, A.V.E. and D.W.B. All authors have read and agreed to the published version of the manuscript.

Funding: The research was supported by the Russian Science Foundation (project No. 22-13-00155).

Institutional Review Board Statement: Not applicable.

Informed Consent Statement: Not applicable.

Data Availability Statement: The main data has been provided in the article and supplementary material. Any other raw/processed data required to reproduce the findings of this study are available from the corresponding author upon request.

Acknowledgments: The authors are thankful to the «Centre for X-ray Diffraction Studies», «Geomodel», «Nanophotonics» and «Nanotechnology» of the Research Park at the Saint Petersburg State University for the helpful assistance in the preparation and characterization of the samples. The electrophysical and electrochemical measurements were carried out using equipment of the laboratory "Photoactive nanocomposite materials" supported by Saint Petersburg State University (ID 94030186).

Conflicts of Interest: The authors declare no conflicts of interest.

References

1. Gabriel, E.; Ma, C.; Graff, K.; Conrado, A.; Hou, D.; Xiong, H. Heterostructure engineering in electrode materials for sodium-ion batteries: Recent progress and perspectives. *eScience* **2023**, *3*, 100139. [CrossRef]
2. Goodarzi, N.; Ashrafi-Peyman, Z.; Khani, E.; Moshfegh, A.Z. Recent progress on semiconductor heterogeneous photocatalysts in clean energy production and environmental remediation. *Catalysts* **2023**, *13*, 1102. [CrossRef]
3. Zhou, W.; Liang, F.; Shao, Z.; Chen, J.; Zhu, Z. Heterostructured electrode with concentration gradient shell for highly efficient oxygen reduction at low temperature. *Sci. Rep.* **2011**, *1*, 155. [CrossRef] [PubMed]
4. Prabhu, P.; Jose, V.; Lee, J.-M. Heterostructured catalysts for electrocatalytic and photocatalytic carbon dioxide reduction. *Adv. Funct. Mater.* **2020**, *30*, 1910768. [CrossRef]
5. Qin, Q.; Sun, M.; Wu, G.; Dai, L. Emerging of heterostructured materials in CO_2 electroreduction: A perspective. *Carbon Capture Sci. Technol.* **2022**, *3*, 100043. [CrossRef]
6. Zhao, G.; Rui, K.; Dou, S.X.; Sun, W. Heterostructures for electrochemical hydrogen evolution reaction: A review. *Adv. Funct. Mater.* **2018**, *28*, 1803291. [CrossRef]
7. Cui, J.; Gibson, U.J. A Simple two-step electrodeposition of Cu_2O/ZnO nanopillar solar cells. *J. Phys. Chem. C* **2010**, *114*, 6408–6412. [CrossRef]

8. Miller, A.M.; Johnson, D.C. Challenges in synthesis of heterostructures. *J. Mater. Chem. C* **2022**, *10*, 6546–6562. [CrossRef]
9. Emeline, A.V.; Rudakova, A.V.; Mikhaylov, R.V.; Bulanin, K.M.; Bahnemann, D.W. Photoactive heterostructures: How they are made and explored. *Catalysts* **2021**, *11*, 294. [CrossRef]
10. Elkholy, A.E.; Duignan, T.T.; Sun, X.; Zhao, X.S. Stable α-MoO_3 electrode with a widened electrochemical potential window for aqueous electrochemical capacitors. *ACS Appl. Energy Mater.* **2021**, *4*, 3210–3220. [CrossRef]
11. Laidoudi, S.; Bioud, A.Y.; Azizi, A.; Schmerber, G.; Bartringer, J.; Barre, S.; Dinia, A. Growth and characterization of electrodeposited Cu_2O thin films. *Semicond. Sci. Technol.* **2013**, *28*, 115005. [CrossRef]
12. Min, C.; Li, S.; Shi, Z.; Xie, J.; Ma, R. Effect of pH on the electrodeposition nucleation and growth mechanism of cuprous oxide. *J. Solid State Electrochem.* **2023**, *27*, 1085–1093. [CrossRef]
13. Neto, V.O.S.; Saraiva, G.D.; Castro, A.J.R.; Freire, P.T.C.; Nascimento, R.F. Electrodeposition of one-dimensional nanostructures: Environmentally friendly method. *J. Compos. Biodegrad. Polym.* **2022**, *10*, 19–42. [CrossRef]
14. Okunaka, S.; Kameshige, H.; Oozu, S.; Yang, Y.; Miyauchi, M.; Tokudome, H. Synthetic strategies of $BiVO_4$ for efficient visible-light-induced photocatalytic oxidation reactions: Activation via nanoparticulation and surface modification. *J. Ceram. Soc. Jpn.* **2023**, *131*, 195–201. [CrossRef]
15. Lai, Y.-H.; Lin, K.-C.; Yen, C.-Y.; Jiang, B.-J. A tandem photoelectrochemical water splitting cell consisting of $CuBi_2O_4$ and $BiVO_4$ synthesized from a single $Bi_4O_5I_2$ nanosheet template. *Faraday Discuss.* **2019**, *215*, 297–312. [CrossRef] [PubMed]
16. Su, Q.; Zuo, C.; Liu, M.; Tai, X. A review on Cu_2O-based composites in photocatalysis: Synthesis, modification, and applications. *Molecules* **2023**, *28*, 5576. [CrossRef] [PubMed]
17. Shi, S.; Xiang, J.; Loy, S.; Meng, X.-S.; Yang, W.-D.; Zhao, R.-D.; Wu, F.-F.; Ma, D.-M.; Li, M.-T.; Li, J. Electrochemical oxygen evolution reaction of controllable self-assembled $CuCo_2O_4$. *Ionics* **2022**, *28*, 4381–4394. [CrossRef]
18. Chen, X.; Zhu, J.-P.; Ding, Y.; Zuo, X.-X. Synthesis of $CuCo_2O_4$ nanoparticles as an anode material with high performance for lithium-ion batteries. *J. Mater. Sci. Mater. Electron.* **2021**, *32*, 18765–18776. [CrossRef]
19. Zheng, J.; Liu, X.; Zhang, L. Design of porous double-shell $Cu_2O@CuCo_2O_4$ Z-scheme hollow microspheres with superior redox property for synergistic photocatalytic degradation of multi-pollutants. *Chem. Eng. J.* **2020**, *389*, 124339. [CrossRef]
20. Sun, J.; Xu, C.; Chen, H. A review on the synthesis of $CuCo_2O_4$-based electrode materials and their applications in supercapacitors. *J. Mater.* **2021**, *7*, 98–126. [CrossRef]
21. Sivashanmugam, G.; Lakshmi, K.; Preethi, B.; Nelson, S.; Sathiyaseelan, M. CTAB-templated formation of $CuCo_2O_4$/CuO nanorods and nanosheets for high-performance supercapacitor applications. *J. Mater. Sci. Mater. Electron.* **2021**, *32*, 27148–27158. [CrossRef]
22. Maevskaya, M.V.; Rudakova, A.V.; Koroleva, A.V.; Sakhatskii, A.S.; Emeline, A.V.; Bahnemann, D.W. Effect of the type of heterostructures on photostimulated alteration of the surface hydrophilicity: TiO_2/$BiVO_4$ vs. ZnO/$BiVO_4$ planar heterostructured coatings. *Catalysts* **2021**, *11*, 1424. [CrossRef]
23. Liang, Y.; Tsubota, T.; Mooij, L.P.A.; van de Krol, R. Highly improved quantum efficiencies for thin film $BiVO_4$ photoanodes. *J. Phys. Chem. C* **2011**, *115*, 17594–17598. [CrossRef]
24. Brandt, I.S.; Tumelero, M.A.; Pelegrini, S.; Zangari, G.; Pasa, A.A. Electrodeposition of Cu_2O: Growth, properties, and applications. *J. Solid State Electrochem.* **2017**, *21*, 1999–2020. [CrossRef]
25. Jayathileke, K.M.D.C.; Siripala, W.; Jayanetti, J.K.D.S. Electrodeposition of p-type, n-type and p-n homojunction cuprous oxide thin films. *Sri Lankan J. Phys.* **2010**, *9*, 35–46. [CrossRef]
26. Wijesundera, R.P.; Gunawardhana, L.K.A.D.D.S.; Siripala, W. Electrodeposited Cu_2O homojunction solar cells: Fabrication of a cell of high short circuit photocurrent. *Sol. Energy Mater. Sol. Cells* **2016**, *157*, 881–886. [CrossRef]
27. Pawar, B.S.; Hou, B.; Ahmed, A.T.A.; Chavan, H.S.; Jo, Y.; Cho, S.; Kim, J.; Seo, J.; Cha, S.N.; Inamdar, A.I.; et al. Facile electrodeposition of high-density $CuCo_2O_4$ nanosheets as a high-performance Li-ion battery anode material. *J. Ind. Eng. Chem.* **2019**, *69*, 13–17. [CrossRef]
28. Wenyan, Z.; Wuyou, F.; Haibin, Y.; Chuanjin, T.; Minghui, L.; Yixing, L.; Lina, Z.; Yongming, S.; Xiaoming, Z.; Hui, C.; et al. Electrodeposition of Cu_2O films and their photoelectrochemical properties. *CrystEngComm* **2011**, *13*, 2871–2877. [CrossRef]
29. De Jongh, P.E.; Vanmaekelbergh, D.; Kelly, J.J. Photoelectrochemistry of electrodeposited Cu_2O. *J. Electrochem. Soc.* **2000**, *147*, 486–489. [CrossRef]
30. Golden, T.D.; Shumsky, M.G.; Zhou, Y.; VanderWerf, R.A.; Van Leeuwen, R.A.; Switzer, J.A. Electrochemical deposition of copper(I) oxide films. *Chem. Mater.* **1996**, *8*, 2499–2504. [CrossRef]
31. Rakhshani, A.E.; Al-Jassar, A.A.; Varghese, J. Electrodeposition and characterization of cuprous oxide. *Thin Solid Films* **1987**, *148*, 191–201. [CrossRef]
32. Wang, L.C.; de Tacconi, N.R.; Chenthamarakshan, C.R.; Rajeshwar, K.; Tao, M. Electrodeposited copper oxide films: Effect of bath pH on grain orientation and orientation-dependent interfacial behavior. *Thin Solid Films* **2007**, *515*, 3090–3095. [CrossRef]
33. Pawar, S.M.; Pawar, B.S.; Babar, P.T.; Ahmed, A.T.A.; Chavan, H.S.; Jo, Y.; Cho, S.; Kim, J.; Hou, B.; Inamdar, A.I.; et al. Nanoporous $CuCo_2O_4$ nanosheets as a highly efficient bifunctional electrode for supercapacitors and water oxidation catalysis. *Appl. Surf. Sci.* **2019**, *470*, 360–367. [CrossRef]
34. De Koninck, M.; Poirier, S.-C.; Marsan, B. $Cu_xCo_{3-x}O_4$ used as bifunctional electrocatalyst: Physicochemical properties and electrochemical characterization for the oxygen evolution reaction. *J. Electrochem. Soc.* **2006**, *153*, A2103–A2110. [CrossRef]

35. Marsan, B.; Fradette, N.; Beaudoin, G. Physicochemical and electrochemical properties of $CuCo_2O_4$ electrodes prepared by thermal decomposition for oxygen evolution. *J. Electrochem. Soc.* **1992**, *139*, 1889–1896. [CrossRef]
36. Wu, L.; Tsui, L.-K.; Swami, N.; Zangari, G. Photoelectrochemical stability of electrodeposited Cu_2O films. *J. Phys. Chem. C* **2010**, *114*, 11551–11556. [CrossRef]
37. Yang, Y.; Han, J.; Ning, X.; Su, J.; Shi, J.; Cao, W.; Xu, W. Photoelectrochemical stability improvement of cuprous oxide (Cu_2O) thin films in aqueous solution. *Int. J. Energy Res.* **2016**, *40*, 112–123. [CrossRef]
38. Kumar, R.; Rai, P.; Sharma, A. Facile synthesis of Cu_2O microstructures and their morphology dependent electrochemical supercapacitor properties. *RSC Adv.* **2016**, *6*, 3815–3822. [CrossRef]
39. Nawaz, B.; Ullah, M.O.; Ali, G. An Investigation of the electrochemical properties of $CuCo_2$ O_4@$NiCo_2O_4$ composite as binder-free electrodes of a supercapacitor. *Energies* **2021**, *14*, 3237. [CrossRef]
40. Yu, Z.; Cheng, Z.; Majid, S.R.; Tai, Z.; Wang, X.; Dou, S. Smart design of free-standing ultrathin Co–$Co(OH)_2$ composite nanoflakes on 3D nickel foam for high-performance electrochemical capacitors. *Chem. Commun.* **2015**, *51*, 1689–1692. [CrossRef]
41. Gautier, J.L.; Trollund, E.; Ríos, E.; Nkeng, P.; Poillerat, G. Characterization of thin $CuCo_2O_4$ films prepared by chemical spray pyrolysis. Study of their electrochemical stability by ex situ spectroscopic analysis. *J. Electroanal. Chem.* **1997**, *428*, 47–56. [CrossRef]
42. Li, G.; Liu, S.; Pan, Y.; Zhou, T.; Ding, J.; Sun, Y.; Wang, Y. Self-templated formation of $CuCo_2O_4$ triple-shelled hollow microspheres for all-solid-state asymmetric supercapacitors. *J. Alloys Compd.* **2019**, *787*, 694–699. [CrossRef]
43. Zhao, Y.-Q.; Zhang, Y.; Xu, K.-Z. Effect of precursor on the morphology and supercapacitor performance of $CuCo_2O_4$. *Int. J. Electrochem. Sci.* **2019**, *14*, 3885–3896. [CrossRef]
44. Jhankal, D.; Khan, M.S.; Yadav, B.; Shakya, P.; Bhardwaj, N.; Jhankal, K.K.; Sachdev, K. Diffusion kinetics of $CuCo_2O_4$ nanorods for next-generation solid state sodium-ion hybrid supercapacitor. *Energy Storage* **2023**, *5*, 482. [CrossRef]